Catalytic degradation of organic pollutants in water under visible light by BiOCl@NH$_2$-MIL-125(Ti–Zr) composite photocatalyst

Zhengming Yu[1], Yunkai Lv[1,*] , Fang Zhang[1], Qi Shi[1], Ke An[1], Feng Huang[1], Tingting Fan[1], Gang Li[2], and Jing Wang[1,2,*]

[1] Present address: Key Laboratory of Analytical Science and Technology of Hebei Province, College of Chemistry and Environmental Science, Hebei University, Baoding 071002, China

[2] Present address: Baoding Green Yijia Environmental Protection Technology Ltd, Baoding 071002, China

ABSTRACT

The pollutant degradation by visible light response photocatalysis is one of the most effective and environmentally friendly strategies, which eagerly expects the highly efficient catalysis. In this study, to incorporate the merits of BiOCl and NH$_2$-MIL-125(Ti–Zr), and exploited their synergistic effect, a series of BiOCl@NH$_2$-MIL-125(Ti–Zr) heterostructures with different NH$_2$-MIL-125(Ti–Zr) contents were fabricated by solvothermal method. The characterization of BiOCl@NH$_2$-MIL-125(Ti–Zr) was performed by XRD, SEM, FTIR, EIS, DRS, and PL. The results showed that NH$_2$-MIL-125(Ti–Zr) bimetallic MOF is highly dispersed on the surface of BiOCl. Compared with the single photocatalyst NH$_2$-MIL-125(Ti-Zr) and BiOCl, the composite photocatalyst BiOCl@NH$_2$-MIL-125(Ti–Zr) demonstrated superior visible light photocatalytic activity. The enhanced performance is ascribed to the improved electron transfer efficiency by NH$_2$-MIL-125(Ti–Zr) bimetallic organic framework and the high dispersion of BiOCl, as well as the formation of heterojunction structure between BiOCl and NH$_2$-MIL-125(Ti–Zr), which separates the photogenerated electron–hole pairs effectively. The optimal content of NH$_2$-MIL-125(Ti–Zr) was 40 wt%, and photocatalytic degradation rate of acid red B(ARB) was up to 89% in 270 min under visible light irradiation. The photocatalytic mechanism was also studied. The results showed that photogenerated hole (h$^+$) and superoxide radical ($\cdot$O$_2^-$) are the main active substances in photocatalytic degradation. After four repeated tests, the composite photocatalyst still has an excellent photocatalytic effect, indicating its high stability and repeatability. This work provides a new idea for the further photocatalytic degradation of pollutants in water.

Address correspondence to E-mail: lvyunkai@126.com; wangjing9804@163.com

 Springer

1 Introduction

With the rapid development of economy and the continuous progress of science and technology, global water pollution has been causing ever-increasing concern [1]. Pollutions in water will not only seriously pollute the environment, destroy the natural ecological balance, but also pose a great threat to people's normal life and health [2, 3]. So, many methods have been studied to solve it, such as adsorption method [4], biological method [5], and photocatalyst method. Adsorption method just shifts pollutants from one medium into another, without fundamentally eliminating organic pollutants [6]. Biological method is strict with reaction condition and not easy to carry out [7]. Photocatalyst method refers to the catalytic degradation of pollutants into non-toxic small molecules or carbon dioxide and water under the synergistic action of light and photocatalyst, which truly achieves the elimination of pollution. Compared with other methods, it has the advantages of free secondary pollution, low energy consumption, and mild reaction conditions [8].

Recently, BiOCl, a new bismuth-based semiconductor, has received dramatic attention concerning applications in the field of catalysis by virtues of excellent stability, good electronic transmission performance, and easy preparation [9–11]. However, BiOCl has an indirect band gap of around 3.2 eV, and only response to UV light, which limits its catalytic performance [12]. At present, the methods to improve the photocatalytic performance of BiOCl mainly include element doping [13], dehalogenation [14], crystal plane controlled [9], build plasma system [15], and construct heterojunction [16]. Heterojunction is the most effective method; Yang Liu and coworkers successfully synthesized Bi_3NbO_7/BiOCl photocatalyst of direct Z-scheme heterojunction; and the apparent rate constant for photocatalytic reduction of Cr(VI) under visible light was 33.2 and 17.6 times as that of Bi_3NbO_7 and BiOCl [17]. As is known to all, specific surface area is an important factor in photocatalytic performance [18, 19]. However, the specific surface area of the heterojunction formed by conventional inorganic photocatalysts was not significantly increased.

Metal-organic frameworks (MOFs) are hybrid materials composed of organic ligands and metal ions, which has clear porosity and large specific surface areas. MOFs have been widely used in gas storage [20], optoelectronic sensors [21], separation [22], Heterogeneous catalysis [23], and other extensive applications. MOFs physical and chemical properties can be adjusted by using different organic ligands or metal ions [24]. Regarding photocatalytic applications, many studies have used NH_2-MIL-125(Ti), which has a band gap of around 2.7 eV, and response to UV light and visible light. In 2019, A. Gómez-Avilés et al. [25] discovered new mixed Ti–Zr MOFs based on NH_2-MIL-125(Ti) with a photocatalytic degradation rate of acetaminophen 1.66 times as high as that of pure NH_2-MIL-125(Ti). However, the rapid recombination of electrons and holes is still an important factor limiting the development of MOFs.

An idea capturing our mind is to incorporate merits of BiOCl and Ti–Zr MOFs to form heterojunction structure, in order to get a synergistic effect. It has been reported in many literatures that the combination of MOFs and inorganic materials can improve the photocatalytic performance. For example, Sheng Yin et al. [26] successfully synthesized the composite photocatalyst Bi_2WO_6@NH_2-MIL-125(Ti), which has much better performance for the photocatalytic degradation of tetracycline hydrochloride than either Bi_2WO_6 or NH_2-MIL-125(Ti).

In this work, a series of BiOCl@NH_2-MIL-125(Ti–Zr) heterostructures with different NH_2-MIL-125(Ti–Zr) contents were directly synthesized via solvothermal. Acid red B has azo groups in its molecular structure, which belongs to azo dyes and commonly exists in waste water. If the public is exposed to azo dyes for a long time, aromatic amines will be generated in the body. The activated aromatic amines can change the DNA structure of the human body, leading to pathological changes or inducing cancer. Thus, the samples were used for degrading organic pollution ARB in water under visible light. The photocatalytic experiment results show that the composite photocatalyst of performance is better than single BiOCl and NH_2-MIL-125(Ti–Zr). The mechanisms of performance improvement were explored. The enhanced performance is ascribed to the heterojunction, which results in the increase of electronic transmission efficiency and the decrease of band gap, as well as the decrease of the recombination rate of electron and hole.
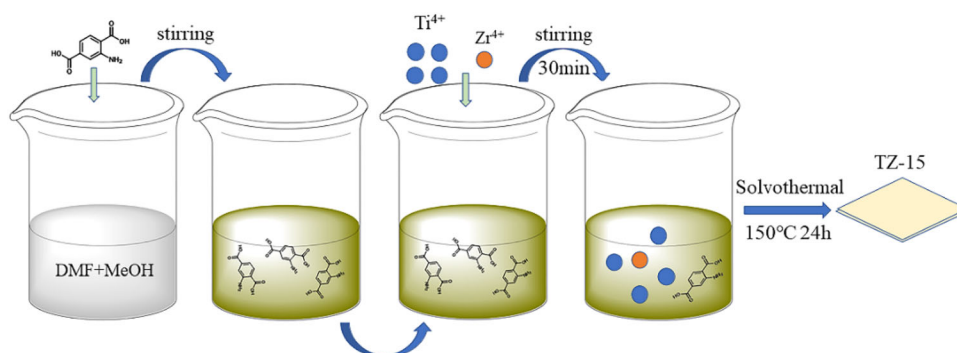
2 Materials and methods

2.1 Reagents

2-aminoterephthalic acid, N,N-dimethylformamide (DMF), titanium isopropoxide, butoxide solution (80 wt% in butanol), ethylene glycol (EG), ethanol (CH_3CH_2OH), methanol (CH_3OH), Bismuth nitrate pentahydrate ($Bi(NO_3)\cdot5H_2O$), potassium chloride (KCl), Isopropanol (IPA), benzoquinone (BQ), and ammonium oxalate (AO) were used. All chemicals used in the experiment were of analytical grade and were used as received without any further purification.

2.2 Preparation of photocatalysts

2.2.1 Synthesis of MOFs

Typically, 0.008 mol of 2-amino-terephthalic acid was added to a 30 ml mixture solution (DMF:MeOH = 4:1) under stirring at room temperature until totally dissolved. Then, 0.002 mol of isopropyl titanate was added to the mixed solution, and continue stirring for 30 min. The mixed solution was transferred to a 100-mL Teflon-lined stainless-steel autoclave, and heated for 24 h at 150 °C, and then cooled naturally to room temperature. The yellow solid was obtained by centrifugation (8000 rpm, 3 min), and then washed with DMF and MeOH. Finally, it was dried for 10 h at 60 °C under vacuum. After drying and grinding, NH_2-MIL-125(Ti) was obtained. The NH_2-MIL-125(Ti–Zr)-X recorded as TZ-X (X represents the mole percentage of zirconium n-butanol in the metal precursor) was synthesized following the same method but with different content isopropyl titanate and zirconium n-butanol. The synthetic route of TZ-15 is shown in Scheme 1.

#### 2.2.2 Synthesis of BiOCl and NH_2-MIL-125(Ti–Zr)@BiOCl

In a typical synthesis, 0.01 mol KCl and a certain amount TZ-15 were added to a solution containing 20 mL of deionized water and 20 ml anhydrous ethanol, stirred for 20 min at room temperature, recorded as solution (A). 0.01 mol Bi(NO3)3·5H2O was added to 40 mL ethylene glycol, stirred for 30 min, and then dispersed by ultrasonic for 20 min, recorded as solution (B). Add solution A to solution B slowly and stirred for 1 h. The mixed solution was transferred to a 100-mL Teflon-lined stainless-steel autoclave and heated for 10 h at 120 °C. The resulting precipitate was collected via centrifugation, washed with anhydrous ethanol and distilled water, and then dried at 80 °C under vacuum overnight. The mass ratio of TZ-15 in the composites is 20%, 30%, 40%, and 50%, which were labeled as BM-20, BM-30, BM-40, and BM-50, respectively. For comparison, pure BiOCl was prepared via the same process omitting the TZ-15. The synthetic route of BM-40 is shown in Scheme 2.

2.3 Characterization

The crystal structures of the samples were determined by X-ray powder polycrystalline diffractometer (XRD; Bruker D8, Germany), using graphite monochromatized Cu Kα radiation, operating at 38 kV and 12 mA. The XRD patterns were obtained in the range of 5–65° (2θ) at a scanning rate of 7° min^{-1}. The microstructures were analyzed by a scanning electron microscope (SEM; JSM-7500 F, Japan). The TEM images of the as-prepared samples were obtained by employing transmission electron microscopy (TEM; JEOL-2100Plus, Japan). The Fourier transform infrared spectroscopy was conducted for the analysis of functional groups in the as-prepared

Scheme 1 The synthetic route of TZ-15 photocatalyst
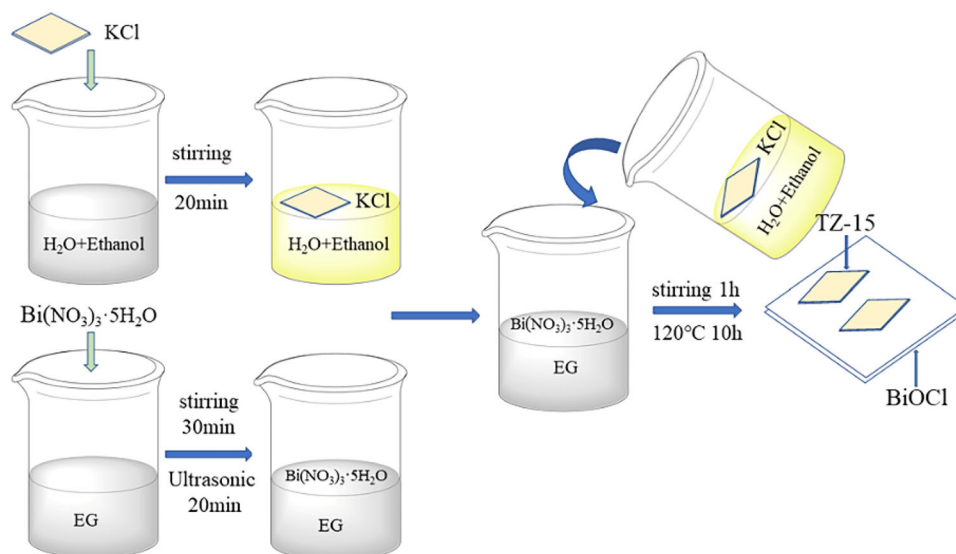
Scheme 2 The synthetic route of BM-40 photocatalyst

samples (FTIR; Thermo Fisher Scientific, Nicolet iS10, America). The UV–Vis diffuse reflectance spectrum of the sample and the absorption spectrum of the dye solution were determined by a near-infrared ultraviolet spectrophotometer (with integrating sphere) manufactured (DRS; UV-3600, Shimadzu, Japan). Photoluminescence experiments to evaluate the electron–hole coincidence rate of photocatalysts were conducted. (PL; Hitachi F-7000, Japan). Electrochemical impedance testing and Mott–Schottky experiments were performed by an electrochemical workstation (EIS; AMETEK Versa STAT 4, America). All tests were performed at room temperature.

2.4 Photocatalytic tests

Typically, 10 mg of the photocatalyst powder was well dispersed in 50 mL ARB (20 mg L^{-1}). Prior to visible light irradiation, the suspension was stirred in the dark for 1 h to achieve an adsorption–desorption equilibrium. The 450 W gold halide lamp equipped with a 420 nm cutoff filter was used as a light source, and keep the temperature constant of 15 °C through circulating cooling water system. At the given intervals, 2.5 mL of the suspension was withdrawn and passed through a 0.22-μm filter to remove the residual photocatalyst particulates. The concentration of the ARB was measured by a UV–Vis spectrophotometer at 516 nm.

3 Results and discussion

3.1 XRD patterns of MOFs

As mentioned earlier, Zr^{4+} doping NH$_2$-MIL-125(Ti) was synthesized by combining isopropyl titanate and zirconium n-butanol in designed ratio in the process of adding the metal precursor. Figure 1 shows the XRD spectra of different TZ MOFs. Characteristic peaks of NH$_2$-MIL-125(Ti) coincide with that
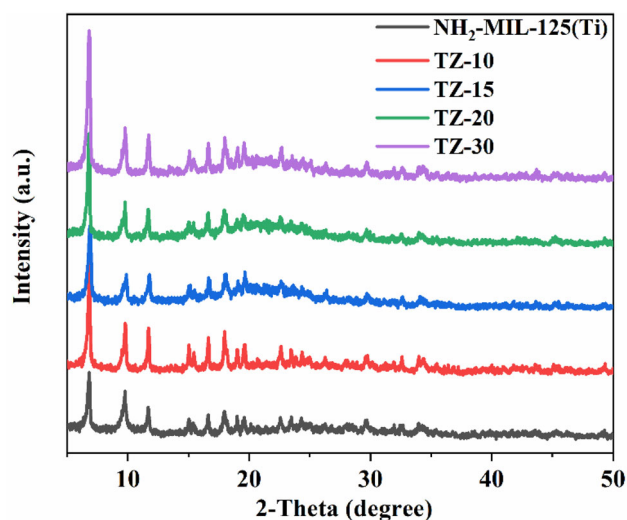

Fig. 1 XRD patterns of NH$_2$-MIL-125(Ti), TZ-10, TZ-15, TZ-20, TZ-30 samples

reported in the literature for NH_2-MIL-125(Ti) and no additional peaks generated, which indicates successful synthesis of NH_2-MIL-125(Ti). Diffraction peaks of TZ-10, TZ-15, TZ-20, and TZ-30 are similar to NH_2-MIL-125(Ti), demonstrating that the existence of Zr^{4+} does not change the lattice construction of NH_2-MIL-125(Ti). It is worth noting that the diffraction peak of NH_2-MIL-125(Ti) at 6.8° is enhanced with the addition of Zr^{4+}. We speculate that the addition of Zr^{4+} promotes the growth of NH_2-MIL-125(Ti) on 002 (6.8°) crystal plane, which leads to the enhancement of diffraction peak.

3.2 SEM and TEM patterns of MOFs

The surface morphology and microstructure of MOFs were investigated by SEM. Figure 2a shows that the NH_2-MIL-125(Ti) performs disk-like shapes and
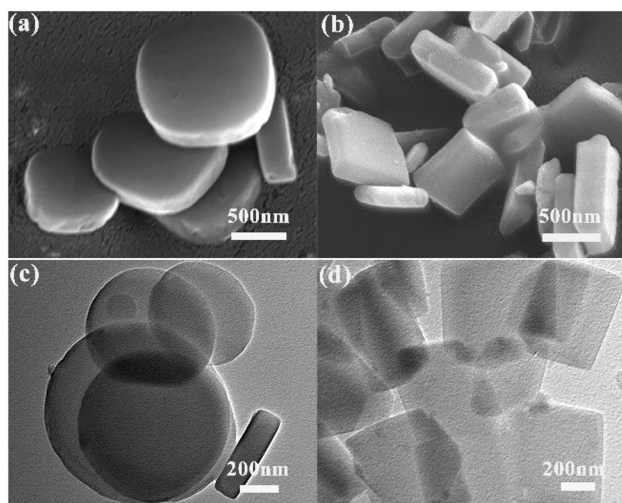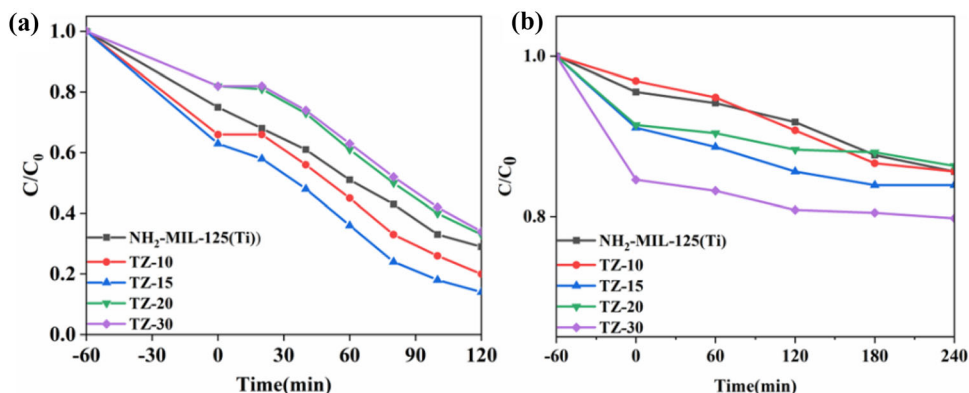

Fig. 2 SEM images of **a** NH_2-MIL-125(Ti), **b** TZ-15, TEM images of **c** NH_2-MIL-125(Ti), **d** TZ-15 samples

smooth surface with an average size of ca. 1 μm, which is identical with the reported literature. The microstructure of NH_2-MIL-125(Ti) has changed with the introduction of Zr. As depicted in Fig. 2b, TZ-15 shows a square shape; however, its average size of ca. 1 μm remains unchanged. To further investigate the morphology and microstructure of the MOFs, TEM was carried out, and the results are shown in Fig. 2c, d. It was further verified that the NH_2-MIL-125(Ti) has smooth surface and disk-like shapes, and the microstructure of TZ-15 has changed, in accordance with SEM analysis results.

3.3 The degradation rate patterns of MOFs

Figure 3 represents the time-course of the RHb and ARB concentration under visible light irradiation with the synthesized TZ MOFs. In the case of NH_2-MIL-125(Ti), only 71% of RHb was photodegraded in 120 min. Significantly, 86% of RHb has been decomposed in the case of TZ-15 within the same irradiation duration. The degradation rate for ARB of photocatalyst TZ-15 and TZ-30 is higher than that of NH_2-MIL-125(Ti), which showed that the doping of Zr^{4+} can improve the photocatalytic performance. Considering the overall performance of degradation rate of the pollutants, the photocatalyst TZ-15 was selected as MOF composition for heterojunction structure.

3.4 SEM and TEM patterns of photocatalysts

The surface morphology and microstructure of samples were investigated by SEM and TEM. Figure 4a shows that the pure BiOCl performs square-like nanoplates with an average size of ca. 100 nm. Furthermore, the square-like nanoplates had smooth surface without adhered impurities, overlapped with

Fig. 3 Degradation rate of **a** RHb and **b** ARB (10 mg photocatalyst; 20 mg L^{-1} pollutant)

Fig. 4 SEM images of **a** BiOCl, **b** BM-40; TEM images of **c** BM-40, **d** EDS elemental mappings of BM-40 sample
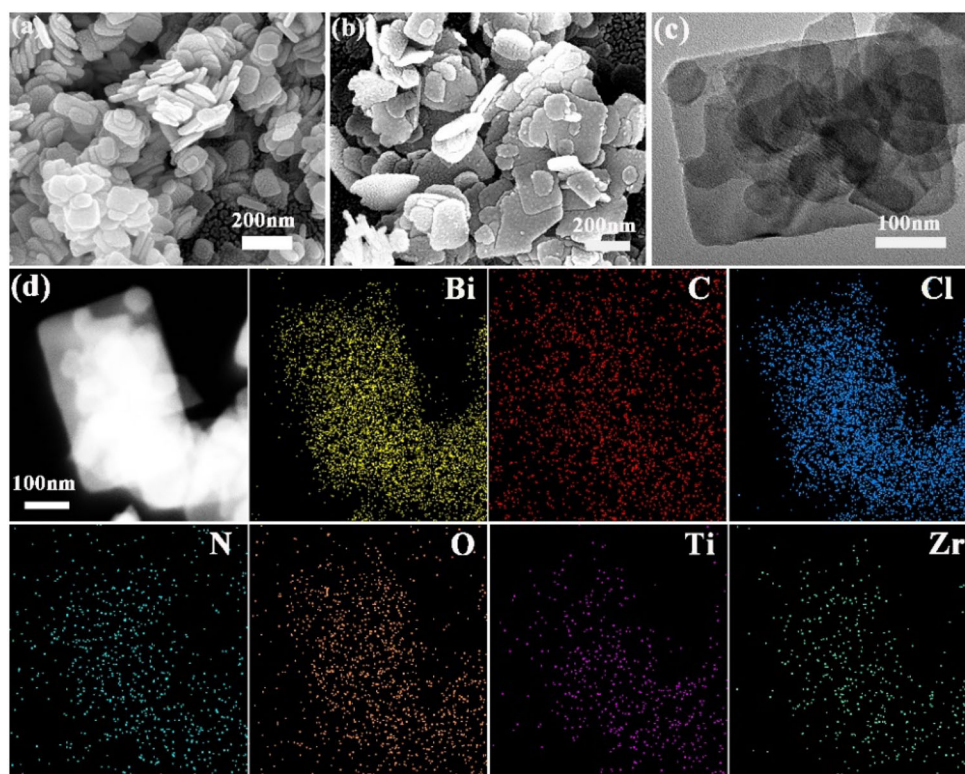
one another, and well dispersion. The morphology of BM-40 is displayed in Fig. 4b, which showed that the TZ-15 was uniformly dispersed on the surface of the BiOCl. In order to understand the microstructure details of the BM-40, TEM and element mapping measurement were carried out, and the results are shown in Fig. 4c, d. Figure 4c confirms that the TZ-15 was dispersed on the surface of BiOCl. And the BM-40 contains element Bi, O, Cl, Ti, Zr, N, and C, determining that the composite photocatalyst was successfully synthesized (Fig. 4d).

3.5 XRD patterns of photocatalysts

Figure 5 shows the XRD patterns of the standard BiOCl card (JCPDS#06-249) and the photocatalyst sample. The synthesized BiOCl is consistent with the standard card, indicating that the BiOCl was successfully synthesized. The main diffraction peaks of BM samples were detected at 11.9°, 25.86°, 32.49°, 33.44°, 41.17°, 46.45°, 54.37°, and 58.6° corresponding to the (001), (101), (110), (102), (112), (200), (211), and (212) crystal planes of BiOCl, respectively. The characteristic peak of TZ-15 was not observed, which may be caused by the low diffraction intensity and high dispersion of TZ-15. This phenomenon can also be
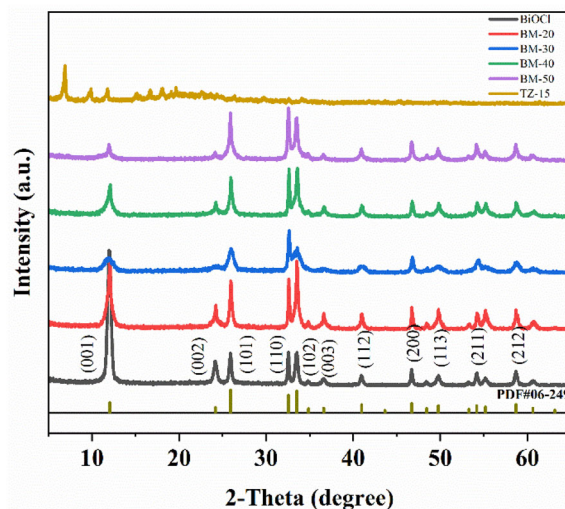

Fig. 5 XRD patterns of BiOCl, TZ-15 and BM samples

observed in other phase systems [27]. It is worth noting that the diffraction peak intensity of BM sample at 11.9° decreases gradually with the increase of TZ-15 content, which may be due to the simple modification of (001) crystal plane of BiOCl by compositing TZ-15. The crystallite size of these photocatalysts was calculated by the method of the Debye-
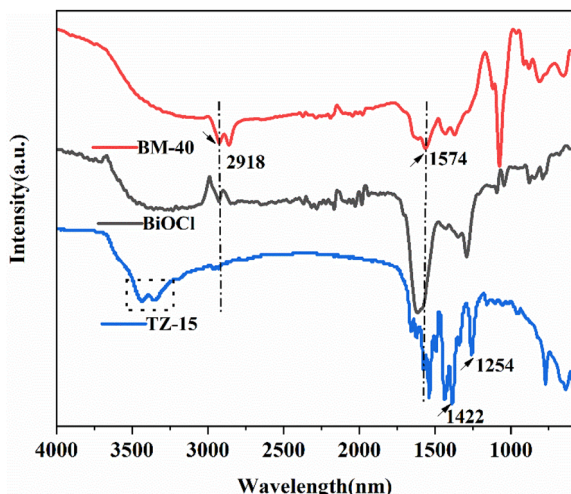
Fig. 6 FTIR spectra of BiOCl, TZ-15, and BM samples

Fig. 7 The UV–Vis absorption spectrum of ARB in water

Scherrer formula, which is based on the following Eq. (1)

$$D = \frac{K\lambda}{\beta cos\theta},$$ (1)

where D is the size of the grain perpendicular to the direction of the crystal plane, β is the full width at half maximum (FWHM) of the measured sample, λ is the wavelength of X-ray (1.54056 Å), θ is Bragg angle, and K is Scherrer's constant (K should be changed to 0.943 for cubic particles). Furthermore, the FWHM should be converted to radian measure. The crystallite size of BiOCl, BM-40, and TZ-15 is 18, 17, and 53 nm, respectively. We speculate that smaller crystallite size leads to the increase of grain boundaries, which is beneficial to the formation of heterojunction and the transfer of electrons, thus improving the photocatalytic performance.

3.6 FTIR spectra of photocatalysts

Figure 6 shows the Fourier transform infrared (FTIR) spectra of the photocatalyst sample. As can be seen from Fig. 6, BiOCl has sharp characteristic peaks at 2918, 1620, and 1290 cm^{-1}. The absorption peak of TZ-15 at 3400–3500 cm^{-1} may be caused by –NH$_2$ stretching in the organic ligand. The absorption peaks at 1100–1800 cm^{-1} are related to the stretching of carboxyl, carbonyl, and phenyl groups. The absorption peaks at 1574 and 1355 cm^{-1} are due to the stretching of –C=C– in the aromatic ring of the ligand [28], The absorption peaks at 1254 and 1422 cm^{-1} are due to the bending of Ti–O–Ti–O and the symmetric
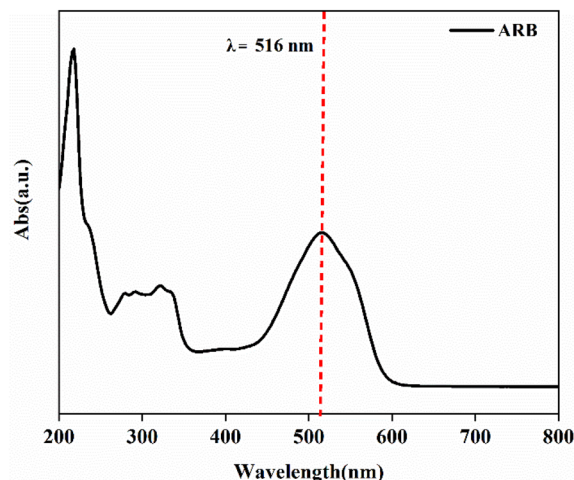
stretching of Zr–O–Zr–O. In the composite photocatalyst BM-40, the characteristic peaks of BiOCl at 2918 cm^{-1} and TZ-15 at 1574 cm^{-1} were observed, indicating that the composite photocatalyst BM was successfully synthesized.

## 3.7 Photocatalytic degradation activity of BM sample

According to Eq. (2): [29]

$$A = kbc$$ (2)

(A is the absorbance, k is the molar absorbance coefficient, and c is the concentration of the light-absorbing substance), absorbance is proportional to concentration, which can be used to calculate the degradation rate of ARB. As can be seen from Fig. 7, ARB has a characteristic absorption peak at 516 nm, caused by the $\pi \rightarrow \pi^*$ transition of the –N=N– bond. Therefore, the absorbance was measured at 516 nm.

Figure 8a shows the degradation of ARB by different photocatalysts. C and C_0 represent the concentration of ARB at time t and initial concentration. After 270 min of visible light irradiation, the degradation rates of TZ-15, BiOCl, BM-20, BM-30, BM-40, and BM-50 were 34%, 12%, 54%, 70%, 87%, 89%, and 86%, respectively. The degradation rate of composite photocatalyst BM is significantly higher than that of pure TZ-15 and BiOCl. With the increase of TZ-15 content, the photocatalytic efficiency increases first and then decreases. The photocatalyst BM-40 with 40% content of TZ-15 has the best catalytic performance, with the highest degradation rate of 89%. It is 2.6 times that of the TZ-15 and 7.4 times that of the

Fig. 8 **a** The photocatalytic degradation process, **b** the detailed absorption spectrum of BM-40, **c** linear fittings of pseudo-first-order, and **d** the reaction rate constants of the composite photocatalysts with different TZ-15 contents
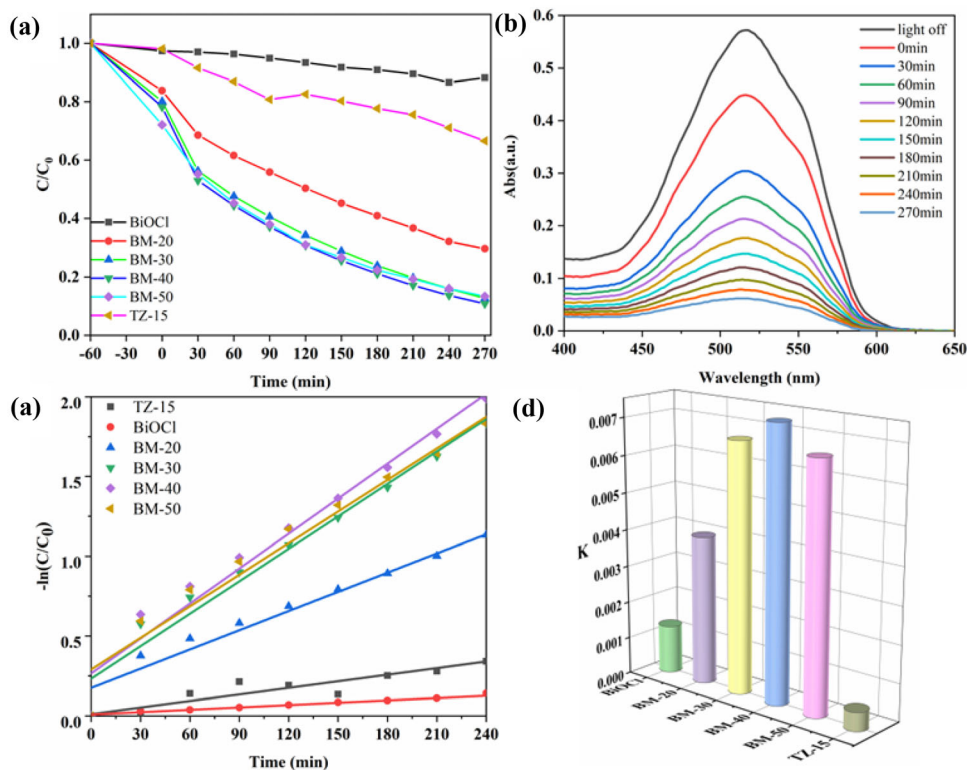
BiOCl. The results show that compositing BiOCl with TZ-15 could improve the performance of the photocatalyst. Figure 8b shows the UV–Vis absorption spectrum of ARB at different reaction times in the presence of BM-40. The UV–Vis absorption spectrum of ARB was measured at 400–650 nm. The absorbance of ARB gradually decreases with the progress of the photocatalytic reaction, indicating that ARB is photocatalyzed and degraded. In addition, the kinetic principle of BM sample degradation of ARB was discussed, and the results are shown in Fig. 8c. $-\ln(C/C_0)$ has a good linear relationship with reaction time t. Thus, it can be determined that the degradation reaction follows the first-order kinetic equation $-\ln(C/C_0) = kt$, where k is the relative reaction rate constant. Figure 8d shows the histogram of reaction rate constants of photocatalyst samples for the degradation of ARB. The values of k of photocatalysts follow the order : BM-40 (7.3×10^{-3} min^{-1}) > BM-30 (6.7×10^{-3} min^{-1}) > BM-50 (6.6×10^{-3} min^{-1}) > BM-20 (4×10^{-3} min^{-1}) > BiOCl (1.3×10^{-3} min^{-1}) > TZ-15 (5×10^{-4} min^{-1}). Thus, BM-40 with 40% TZ-15 content has the highest photocatalytic performance.

3.8 Stability analysis of photocatalytic performance

The stability and reusability of photocatalyst are also an important factor to evaluate the performance of the photocatalyst, which determines whether the photocatalyst can be applied in practice. Therefore, a four-cycle test was carried out to assess the efficiency of ARB. It can be seen that the photocatalytic activity of BM-40 is only about 8% loss after four cycles, and the photodegradation efficiency is still maintaining more than 80% (Fig. 9), demonstrating the as-obtained BM-40 photocatalyst has good stability during the photoreduction reaction process. The reduction of photocatalytic activity may be caused by the loss of photocatalyst in the washing process.

To further verify the stability of the photocatalyst, we tested the BM-40 after circulation by XRD. As can be seen from Fig. 10, the diffraction peak position of BM-40 does not shift obviously except the intensity decreases after four cycles of testing, which proves the sample has excellent stability in the reaction process.

3.9 Study on photocatalytic mechanism

Fig. 11a shows the UV–Vis diffuse reflection pattern of the photocatalyst sample. The pure BiOCl sample has an apparent absorption band edge around 350 nm, corresponding to UV region, while the absorption band edge of TZ-15 is around 500 nm, involving the UV and visible light region. Furthermore, two absorption peaks around 280 and 390 nm belonging to the metal precursor and amine ligand can be observed. Notably, after combining BiOCl with TZ-15, the composite photocatalyst BM manifests favorable optical response. Meanwhile, BM-40

and BM-50 have a new peak belonging to amine ligand of TZ-15, which indicates the composite photocatalyst BM was successfully synthesized. The band gap energy of these photocatalysts was calculated by the method of Tauc plot, which is based on the following Eq. (3)

$$\alpha h\upsilon = A\left(h\upsilon - E_g\right)^{n/2}, \qquad (3)$$

where α is the absorption coefficient, h denotes the Planck's constant, υ means the light frequency, and A corresponds to constant. Since the composite photocatalyst BM prepared is an indirect band gap material, $n = 4$. As can be seen from Fig. 11b, the band gaps of TZ-15, BiOCl, BM-20, BM-30, BM-40, and BM-50 are 2.337, 3.183, 2.733, 2.19, 2.879, and 1.796 eV, respectively. The band gaps of BM were smaller than those of BiOCl, and the narrower band
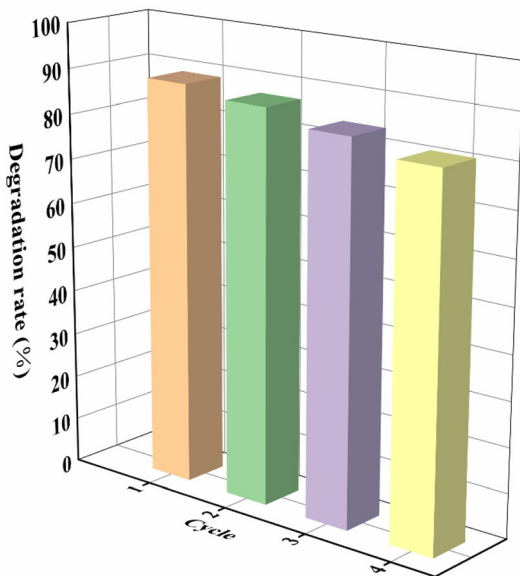

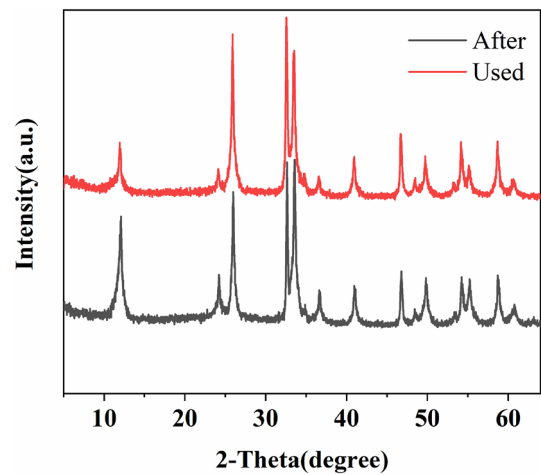Fig. 9 The reusability and photocatalytic stability test of the BM-40 photocatalyst

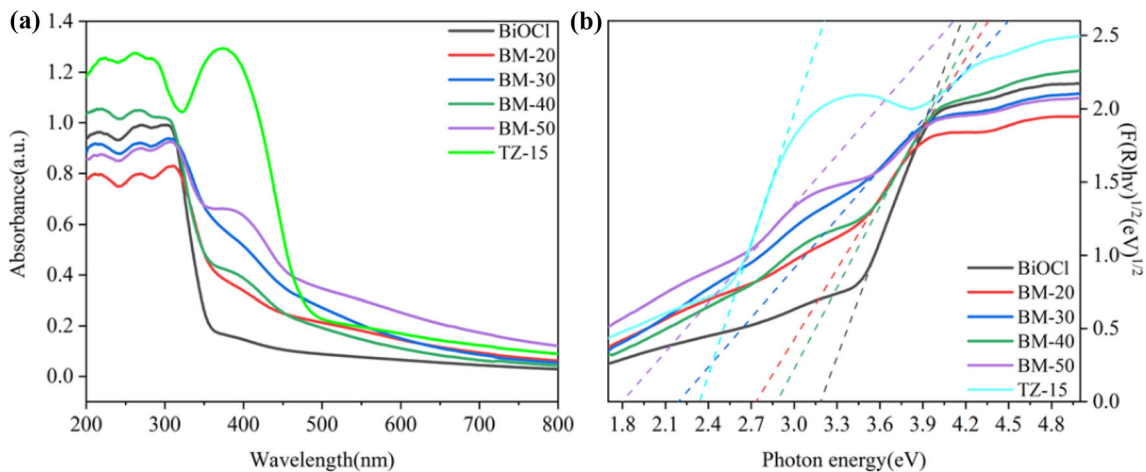Fig. 10 XRD pattern of BM-40 after the three successive runs

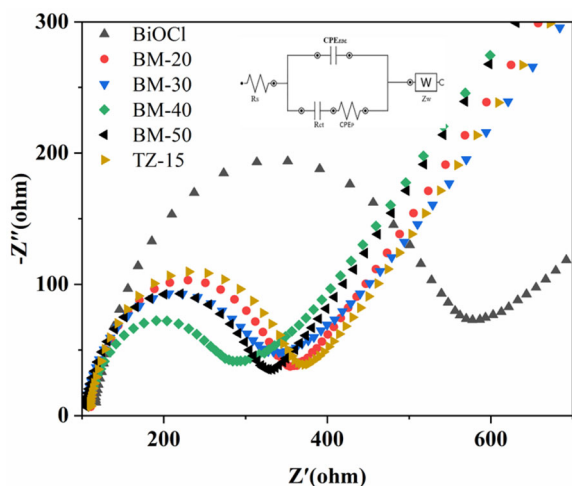Fig. 11 a UV–Vis diffuse reflectance spectra and b the corresponding band energy diagram
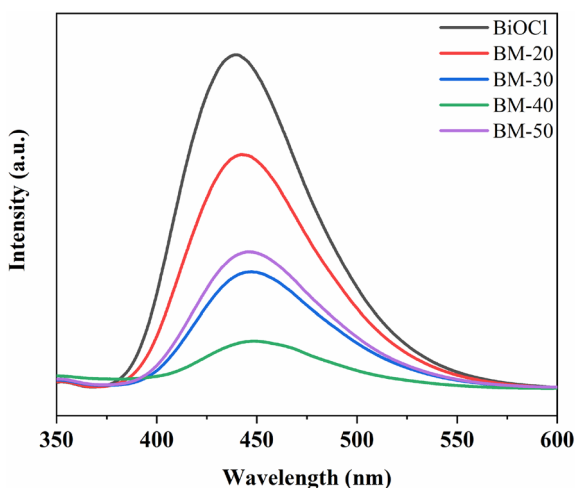
Fig. 12 EIS Nyquist of photocatalysts

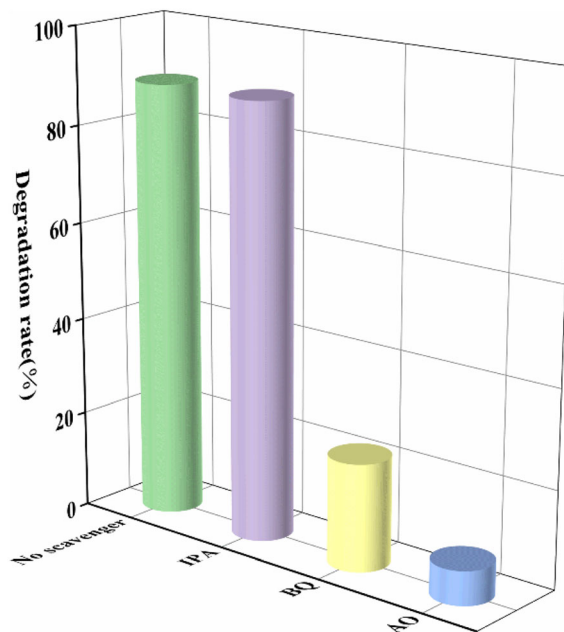**Fig. 13** PL spectra of photocatalysts

Fig. 14 Photocatalytic degradation rate of ARB in different scavengers

372.5 Ω), which indicates the good electron transfer of BM-40 during photocatalytic ARB reduction.

It is well known that the electron–hole coincidence rate is also an important factor affecting the photocatalytic performance. The composite BM in the photodegradation systems was investigated based on the photoluminescence (PL) spectra. It is generally believed that weaker intensity represents lower recombination probability of photogenerated charge carriers. All photocatalysts show certain fluorescence at 450 nm under the excitation wavelength of 315 nm (Fig. 13). The introduction of TZ-15 to the BiOCl obviously decreases the PL intensity, which proves that the recombination of the photogenerated charge carriers in BiOCl is achieved through the formation of heterojunction between TZ-15 and BiOCl.

With the goal to achieve a better understanding of the photocatalytic mechanism of the composite BM, the scavenger experiments were conducted by adding individual scavengers in the degradation experiment. Isopropanol (IPA) was used for quenching hydroxyl radicals ($\cdot$OH), benzoquinone (BQ) for superoxide radicals ($\cdot O_2^-$), and ammonium oxalate (AO) for photogenerated holes (h^+), respectively [30–32]. As shown in Fig. 14, the photocatalytic performance is inhibited significantly after the introduction of BQ and AO, while the addition of IPA

gap is beneficial to provide more photogenerated charge carriers, which were crucial to improve catalytic efficiency.

In order to get more insights into the separation efficiency of the photogenerated charge carriers of the composite BM, the electrochemical impedance spectroscopy (EIS) of the as-prepared samples was also recorded. The radius of the arc represents the resistance of the photocatalyst. The smaller the radius, the smaller the resistance, so it is easier for the electrons to transfer. As shown in Fig. 12, the Nyquist plot of composite BM-40 exhibits the smaller semicircular, and the resistance of composite BM-40 (285.7 Ω) is the lowest among that of all photocatalyst (BiOCl 332.2 Ω, BM-20 357.7 Ω, BM-30 334.1 Ω, BM-50 572.2 Ω, TZ-15

Fig. 15 Schematic diagram of photocatalytic mechanism of BM-40 under visible light irradiation
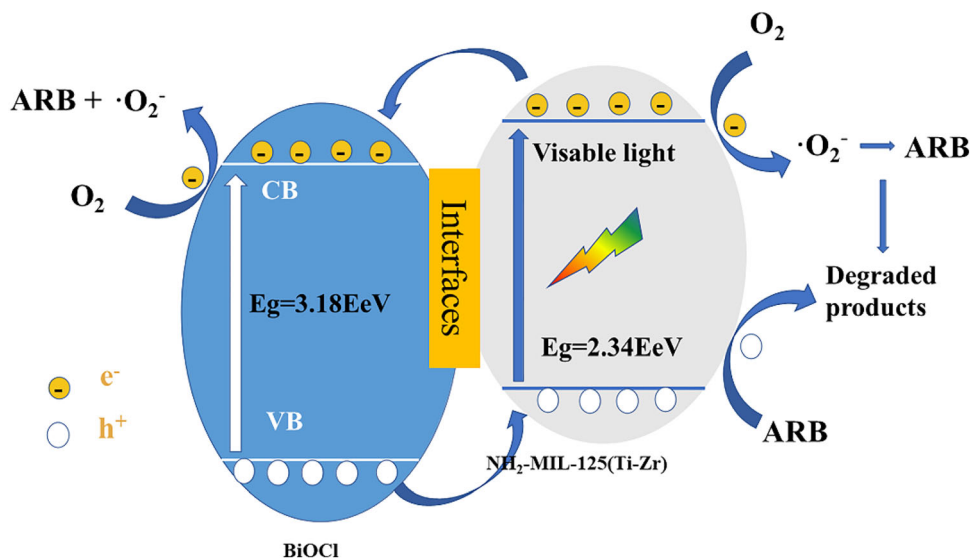
exerts little influence on the photocatalytic activity. It is assumed that the crucial role is $\cdot O_2^-$ and h^+ toward photodegradation of ARB instead of $\cdot OH$.

Based on the above analysis, a probable mechanism over BM-40 photocatalytic of ARB was discussed. As illustrated in Fig. 15, under visible light irradiation, electrons in the valence band (VB) of TZ-15 and BiOCl are photoexcited to the conduction band (CB) separately. Amount of photogenerated electrons in the CB of TZ-15 can be transferred to the CB of BiOCl, and the h^+ in the VB of BiOCl to the VB of the TZ-15 through the heterojunction interface. This process reduces the recombination of photogenerated electrons and holes, and improves the catalytic performance. The photogenerated electrons can capture oxygen molecules (O_2) in the solution to yield $\cdot O_2^-$, which can further react with ARB molecules, and the h^+ at the TZ-15 can react directly with ARB molecules.

4 Conclusions

In summary, a highly efficient photocatalyst BiOCl@NH$_2$-MIL-125(Ti–Zr) was successfully synthesized via the hydrothermal method. The composite BM-40 exhibited more than 85% ARB degradation efficiency under visible light within 270 min. And its photocatalytic activity is much higher than that of the pure BiOCl and NH$_2$-MIL-125(Ti–Zr)-15. Heterojunction between BiOCl and NH$_2$-MIL-125(Ti–Zr) strengthens the photogenerated

charge separation, visible light responsibility, and electron transfer efficiency, which is the reason for improvement of photocatalytic performance. The degradation mechanism of ARB demonstrates that $\cdot O_2^-$ and h^+ are the dominant reactive radical. After four recycles, the BM-40 still had an excellent performance. Overall, this study offers valuable insights onto the degradation of organic dyestuff.

Author contributions

ZY: Writing—original draft, Investigation. YL: Formal analysis. FZ: Investigation. QS: Investigation. KA: Investigation. FH: Investigation. TF: Investigation. GL: Funding acquisition. JW: Funding acquisition, Formal analysis.

Funding

Data availability

All data included in this study are available upon request by contact with the corresponding author.

Code availability

Not applicable.

Declarations

Conflict of interest We declare that we have no financial and personal relationships with other people or organizations that can inappropriately influence our work. There is no professional or other personal interest of any nature or kind in any product, service and/or company that could be construed as influencing the position presented in, or the review of, the manuscript entitled, "Catalytic degradation of organic pollutants in water under visible light by BiOCl@NH$_2$-MIL-125(Ti–Zr) composite photocatalyst."

Ethical approval Hereby, we declare that the manuscript is our original work and not has been published or under editorial considerations anywhere else. The stated authors of the work have read the content and approved for submission of this manuscript to Journal of Materials Science: Materials in Electronics. There is no personal or financial conflict of interest. Further if our article has been accepted, we ensure that we will not publish it anywhere else in any form, in any language without getting consent of the publisher.

References

1. S. Mao, J. Chang, G. Zhou, J. Chen, Nanomaterial-enabled rapid detection of water contaminants. Small **11**, 5336–5359 (2015)

2. A.A. Zewde, L. Zhang, Z. Li, E.A. Odey, A review of the application of sonophotocatalytic process based on advanced oxidation process for degrading organic dye. Rev. Environ. Health **34**, 365–375 (2019)

3. K. Qi, M. Song, M. Xie, Y. Wen, Z. Wang, B. Wei, Z. Wang, CQDs/biochar from reed straw modified Z-scheme MgIn$_2$S$_4$/BiOCl with enhanced visible-light photocatalytic performance for carbamazepine degradation in water. Chemosphere **287**, 132192 (2021)

4. V.R. Kesamseetty, R. Singampalli, A. BabuTadiboyina, V.K.P. Narasipuram, K.V. Prasad, M. Hanumanthrayappa, V.N. Ratnakaram, J. Sannapaneni, C.B.N. Kadiyala, Role of carbon materials in the removal of organic pollutants: an abridged review. Biointerface Res. Appl. Chem. **12**, 1974–1997 (2022)

5. B. Wang, J. Xu, J. Gao, X. Fu, H. Han, Z. Li, L. Wang, Y. Tian, R. Peng, Q. Yao, Construction of an *Escherichia coli* strain to degrade phenol completely with two modified metabolic modules. J. Hazard. Mater. **373**, 29–38 (2019)

6. L. Li, D. Zou, Z. Xiao, X. Zeng, L. Zhang, L. Jiang, A. Wang, D. Ge, G. Zhang, F. Liu, Biochar as a sorbent for emerging contaminants enables improvements in waste management and sustainable resource use. J. Clean. Prod. **210**, 1324–1342 (2019)

7. P. Bhatt, S. Gangola, G. Bhandari, W. Zhang, D. Maithani, S. Mishra, S. Chen, New insights into the degradation of synthetic pollutants in contaminated environments. Chemosphere **268**, 128827 (2021)

8. W.S. Koe, J.W. Lee, W.C. Chong, Y.L. Pang, L.C. Sim, An overview of photocatalytic degradation: photocatalysts, mechanisms, and development of photocatalytic membrane. Environ. Sci. Pollut Res. **27**, 2522–2565 (2020)

9. C. Liu, Y. Ren, Z. Wang, Y. Shi, B. Guo, Y. Yu, L. Wu, Flowerlike BiOCl nanospheres fabricated by an in situ self-assembly strategy for efficiently enhancing photocatalysis. J. Colloid Interface Sci. **607**, 423–430 (2022)

10. M. Liu, H. Zhu, N. Zhu, Q. Yu, Vacancy engineering of BiOCl microspheres for efficient removal of multidrug-resistant bacteria and antibiotic-resistant genes in wastewater. Chem. Eng. J. **426**, 130710 (2021)

11. J. Liu, Y. Li, L. Huang, C. Wang, L. Yang, J. Liu, C. Huang, Y. Song, Fabrication of novel narrow/wide band gap Bi$_4$O$_5$I$_2$/BiOCl heterojunction with high antibacterial and degradation efficiency under LED and sunlight. Appl. Surf. Sci. **567**, 150713 (2021)

12. M. Nafradi, K. Hernadi, Z. Konya, T. Alapi, Investigation of the efficiency of BiOI/BiOCl composite photocatalysts using UV, cool and warm white LED light sources—photon efficiency, toxicity, reusability, matrix effect, and energy consumption. Chemosphere **280**, 130636 (2021)

13. Z. Long, H. Wang, K. Huang, G. Zhang, H. Xie, Di-functional Cu(2+)-doped BiOCl photocatalyst for degradation of organic pollutant and inhibition of cyanobacterial growth. J. Hazard. Mater. **424**, 127554 (2021)

14. X. Xiao, C. Liu, R. Hu, X. Zuo, J. Nan, L. Li, L. Wang, Oxygen-rich bismuth oxyhalides: generalized one-pot synthesis, band structures and visible-light photocatalytic properties. J. Mater. Chem. **22**, 22840 (2012)

15. M.Y. Liu, G.L. Lin, Y.M. Liu, X.Y. Lin, L.J. Wang, Y.F. Xu, X.C. Song, Ternary heterojunction Ag/AgIO₃/BiOCl(CMC) by a biomass template for photodegradation of tetracycline hydrochloride and gaseous formaldehyde. Solid State Sci. **112**, 106517 (2021)

16. H. Wang, B. Liao, T. Lu, Y. Ai, G. Liu, Enhanced visible-light photocatalytic degradation of tetracycline by a novel hollow BiOCl@CeO₂ heterostructured microspheres: structural characterization and reaction mechanism. J. Hazard. Mater. **385**, 121552 (2020)

17. Y. Liu, J. Xu, M. Chen, Synthesis of direct Z-scheme Bi₃₋NbO₇/BiOCl photocatalysts with enhanced activity for CIP degradation and Cr(VI) reduction under visible light irradiation. Sep. Purif. Technol. **276**, 119255 (2021)

18. C. Hu, Y.R. Lin, H.C. Yang, Recent developments in graphitic carbon nitride based hydrogels as photocatalysts. ChemSusChem **12**, 1794–1806 (2019)

19. T. Sato, P. Zhang, S. Yin, High performance visible light responsive photocatalysts for environmental cleanup via solution processing. Prog. Cryst. Growth Ch. Mater. **58**, 92–105 (2012)

20. A.R. Millward, O.M. Yaghi, Metal-organic frameworks with exceptionally high capacity for storage of carbon dioxide at room temperature. J. Am. Chem. Soc. **127**, 17998–17999 (2005)

21. D. Jin, Q. Xu, L. Yu, X. Hu, Photoelectrochemical detection of the herbicide clethodim by using the modified metal-organic framework amino-MIL-125(Ti)/TiO₂. Microchim. Acta. **182**, 1885–1892 (2015)

22. J. Yao, H. Wang, Zeolitic imidazolate framework composite membranes and thin films: synthesis and applications. Chem. Soc. Rev. **43**, 4470–4493 (2014)

23. J. Qiu, X.F. Zhang, X. Zhang, Y. Feng, Y. Li, L. Yang, H. Lu, J. Yao, Constructing Cd₀.₅Zn₀.₅S@ZIF-8 nanocomposites through self-assembly strategy to enhance Cr(VI) photocatalytic reduction. J. Hazard. Mater. **349**, 234–241 (2018)

24. T. Devic, C. Serre, High valence 3p and transition metal based MOFs. Chem. Soc. Rev. **43**, 6097–6115 (2014)

25. A. Gómez-Avilés, M. Peñas-Garzón, J. Bedia, D.D. Dionysiou, J.J. Rodríguez, C. Belver, Mixed Ti-Zr metal-organic-frameworks for the photodegradation of acetaminophen under solar irradiation. Appl. Catal. B Environ. **253**, 253–262 (2019)

26. S. Yin, Y. Chen, Q. Hu, M. Li, Y. Ding, J. Di, J. Xia, H. Li, Construction of NH₂-MIL-125(Ti) nanoplates modified Bi₂WO₆ microspheres with boosted visible-light photocatalytic activity. Res. Chem. Intermed. **46**, 3311–3326 (2020)

27. S.R. Zhu, P.F. Liu, M.K. Wu, W.N. Zhao, G.C. Li, K. Tao, F.Y. Yi, L. Han, Enhanced photocatalytic performance of BiOBr/NH₂-MIL-125(Ti) composite for dye degradation under visible light. Dalton Trans. **45**, 17521–17529 (2016)

28. S. Hu, M. Liu, K. Li, Y. Zuo, A. Zhang, C. Song, G. Zhang, X. Guo, Solvothermal synthesis of NH₂-MIL-125(Ti) from circular plate to octahedron. CrystEngComm **16**, 9645–9650 (2014)

29. H.Y. Gu, W.S. Chang, Three-dimensional protein shape rendering in magnetized solution with Lambert-Beer law. Appl. Opt. **51**, 4827–4832 (2012)

30. J. Di, J. Xia, M. Ji, B. Wang, S. Yin, Q. Zhang, Z. Chen, H. Li, Carbon quantum dots modified BiOCl ultrathin nanosheets with enhanced molecular oxygen activation ability for broad spectrum photocatalytic properties and mechanism insight. ACS Appl. Mater. Interfaces **7**, 20111–20123 (2015)

31. L. Ye, J. Liu, Z. Jiang, T. Peng, L. Zan, Facets coupling of BiOBr-g-C₃N₄ composite photocatalyst for enhanced visible-light-driven photocatalytic activity. Appl. Catal. B Environ. **142–143**, 1–7 (2013)

32. M.C. Yin, Z.S. Li, J.H. Kou, Z.G. Zou, Mechanism investigation of visible light-induced degradation in a heterogeneous TiO₂/Eosin Y/Rhodamine B system. Environ. Sci. Technol. **43**, 8361–8366 (2009)